Article

Not peer-reviewed version

Automatic Multi-Temporal Land Cover Mapping with Fine Spatial Resolution Using the Model Migration Method

Ruijun Chen , Xidong Chen * , Yu Ren

Posted Date: 18 October 2024

doi: 10.20944/preprints202410.1402.v1

Keywords: time series; land cover; remote sensing classification; classification model migration; Landsat

doi:10.20944/preprints202410.1402.v1

Article

Automatic Multi-Temporal Land Cover Mapping with Fine Spatial Resolution Using the Model Migration Method

Ruijun Chen [1], Xidong Chen [2]*, Yu Ren [3, 4]

[1] Faculty of Architecture, The University of Hong Kong, Hong Kong SAR 999007, China
[2] Future Urbanity & Sustainable Environment (FUSE) Lab, Division of Landscape Architecture, Department of Architecture, Faculty of Architecture, The University of Hong Kong, Hong Kong SAR 999007, China
[3] Key Laboratory of Ecological Safety and Sustainable Development in Arid Lands, Northwest Institute of Eco-Environment and Resources, Chinese Academy of Sciences, Lanzhou 730000, China
[4] University of Chinese Academy of Sciences, Beijing 100049, China
* Correspondence: xdchenrs@hku.hk

Abstract: Land cover refers to the combination of various material types and their natural characteristics on the Earth. Accurately mapping the spatial distribution and temporal changes of the earth's land cover is of great significance for studying the energy balance and carbon cycle of the earth system. However, there is still a high degree of human participation in the production of multi-temporal land cover products. Developing an automated method for multi-epoch land cover mapping has become a key research focus. To this end, an automatic training sample extraction method was first employed using multi-source prior land cover products. Then, based on the generated training dataset and the Random Forest classifier, local adaptive land cover classification models of the reference year were developed. Finally, by migrating the classification model to the target epoch, the multi-epoch land cover products were generated. Yuli County in Xinjiang and Linxi County in Inner Mongolia were used as test cases. The classification models were first generated in 2020 and then transferred to 2010 to enable automatic classification of multi-temporal land cover. The mapping results showed high accuracy in both regions, with Yuli County achieving 92.52% in 2020 and 88.33% in 2010, and Linxi County achieving 90.28% in 2020 and 85.28% in 2010. Additionally, uncertainty analysis of the model migration method revealed that land types such as water bodies, wetlands, and impervious surfaces, which exhibit significant spectral changes over time, are less suitable for the model migration. Our research can offer valuable insights for fine-resolution land cover mapping. Furthermore, the approach provides a scalable solution for multi-period land cover monitoring, which could facilitate more efficient and accurate environmental assessments.

Keywords: time series; land cover; remote sensing classification; classification model migration; Landsat

---

1. Introduction

Land cover refers to the composition of various material types and their natural properties on the surface of the Earth. Its spatial distribution and migration play a crucial role for the balance of the water, heat, and material at the surface [1]. Changes in land cover not only impact biogeochemical cycles but also lead to climate change potentially [2]. Therefore, for developing the study of the energy balance, carbon cycle, biogeochemical processes, and climate change within the Earth system, it is very important to determine the spatial distribution and temporal dynamics of land cover accurately.

With its large-scale observational capabilities and repeatability, remote sensing technology offers significant advantages for land cover classification and mapping [3]. For example, Hansen et al. (2000) produced a global 1-km land cover product (UMD) by AVHRR data [4]. The European Space Agency (ESA) developed the 300-m global land coverage product GlobCover based on MERIS data [5]. The National Aeronautics and Space Administration (NASA) created a global 500-m resolution land-cover product (MODIS land-cover product, MCD12Q1) with MODIS data [6]. ESA later advanced the field with a 300-m global land-cover product (ESA Climate Change Initiative Global Land Cover, CCI_LC) based on multi-source remote sensing data [7].

In recent years, the availability of fine-resolution (10 m-100 m) remote sensing data, such as Sentinel-2 and the Landsat series, has spurred significant advances in land cover research, primarily through open data sharing [8]. These datasets provide enhanced texture details and spatial structure information and enable a more detailed understanding of land cover changes. As a result, fine-resolution land cover mapping has gained increasing attention among researchers. For example, Gong et al. developed a global 30-meter land-cover product using supervised classification based on a global training sample set [9]. Chen et al. also produced a high-precision 30-m global land cover product (GlobLand30) by combining visual interpretation and supervised classification [10]. However, these fine-resolution products heavily rely on manual efforts to obtain training data, which will make it challenging to update the products efficiently. As the need for dynamic land cover monitoring grows, there is increasing interest in developing methods for the rapid categorization, mapping, and updating of fine-resolution land cover products over different regions and years [11].

To address the limitations of traditional supervised classification, which requires significant manual labor for constructing training sample sets, researchers have explored automated methods for generating these datasets using existing land cover data. For instance, Radoux et al. (2014) developed a 300-m land cover product for Eurasia and South America by automatically extracting high-confidence training samples from CCI_LC [12]. Zhang et al. (2017) utilized MODIS land cover products to automate training data generation for classifying Landsat data [13]. Moreover, Liu et al. proposed an approach that leverages existing land cover products and MODIS surface reflectance data to construct a geoid time-series spectral library [14]. It produced 30-meter time-series spectral libraries for China and global regions [15,16]. Although these studies demonstrate the feasibility of automatically generating and classifying training data from existing land cover products, the strategy is typically applied to the development of single-period land cover products. This is because the mapping year must closely match the year of the land cover product used. Consequently, constructing classification models that can be applied across different periods remains a critical challenge in producing multi-period land cover products [17].

In response to this challenge, a novel classification strategy based on the extension of classification models has emerged in recent studies on automated land cover mapping [18]. This approach is predicated on the assumption that images of the same surface feature at different times exhibit similar or identical reflectance spectra. Therefore, by extending classification models trained on spectral data to images from various years, multi-year land cover information can be automatically extracted [19,20]. Building upon this idea, this study integrates 30-meter multi-source land cover products with a classification model expansion strategy, which aims to automatically identify and monitor land cover elements in Yuli County, Xinjiang, and Linxi County, Inner Mongolia, as case studies. The approach involves developing an automated method to extract training data from existing multi-source land cover products to create a high-precision training dataset. Spectral features from time-series Landsat images of the base year for each region are then extracted, and the generated training dataset is used to build a land cover classification model. This model is subsequently expanded to target years in each region. It enables the rapid identification and extraction of multi-year land cover information at a fine resolution. This methodology offers valuable insights and potential solutions for the automated monitoring of land cover elements.

2. Study Area and Data

2.1. Study Area

This study focuses on two diverse regions: Yuli County in Xinjiang and Linxi County in Inner Mongolia (Figure 1). These areas present distinct climatic conditions and topographical features, which located in the northwest and northeast of China, respectively. It offers an ideal setting to evaluate the robustness of the proposed classification algorithm under varying environmental conditions. Both regions benefit from Landsat ETM+/OLI imagery with minimal cloud interference, and their high-latitude location ensures a greater degree of image overlap [15]. These characteristics provide ample valid observations, which are essential for land cover monitoring. The predominant landscapes in Yuli and Linxi counties include mountains, plains, and deserts, with a diverse range of land cover types such as cropland, forestland, shrubland, grassland, waterbody, bare land, impervious surface, and wetlands. These varied landforms make the regions ideal for land cover studies.

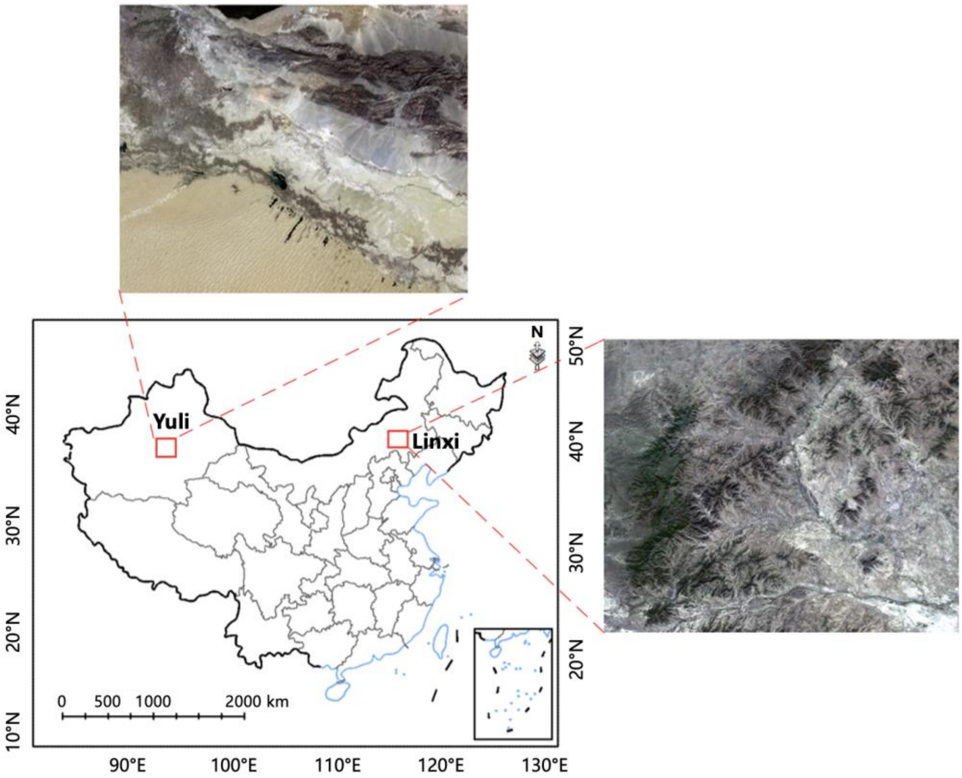

Figure 1. The location of Yuli County area, Xinjiang and Linxi County area, Inner Mongolia.

2.2. Remote Sensing Imagery and Data Preprocessing

This study conducts automated land cover classification with time-series Landsat OLI and ETM+ surface reflectance data from 2020 ± 1 year and 2010 ± 1 year. Notably, the Coastal band from the OLI sensor is excluded from the analysis due to its high sensitivity to atmospheric conditions, which makes it unsuitable for time-series remote sensing studies [21–23]. The analysis includes the 15-meter panchromatic bands from OLI and ETM+, which enhance spatial details and are particularly useful for detecting fine features like towns and rivers [22,23]. To maximize classification accuracy, only images with less than 80% cloud cover were selected. Cloud and cloud shadow pixels were masked using data from the cloud detection files in the Landsat QA layer [24]. The specific Landsat OLI and ETM+ bands utilized in this study are outlined in Table 1.

Table 1. Load setting of Landsat OLI and Landsat ETM+.

Band	Landsat OLI band	OLI band range (nm)	Landsat ETM+ band	ETM+ band range (nm)
Blue	2	450-515	1	450-520
Green	3	525-600	2	520-600
Red	4	630-680	3	630-690
NIR	5	845-885	4	770-900
SWIR1	6	1560-1660	5	1550-1750
SWIR2	7	2100-2300	7	2080-2350
Panchromatic	8	500-900	8	520-900

2.3. Land Cover Reference Data

Among the available high-resolution land cover products, GlobeLand30 is one of the most extensively utilized global datasets with a 30-meter resolution [14,25]. Developed by the National Geomatics Center of China, GlobeLand30 is based on Landsat imagery and uses a combination of object-oriented classification and manual interpretation. The overall mapping accuracy of this product reaches 83.50%, with a Kappa coefficient of 0.78, which positions it as one of the most accurate global land cover products available [10]. GlobeLand30 has been released in three phases—2000, 2010, and 2020. With the superior mapping accuracy of the 2020 dataset, this study references its results to extract a high-confidence training sample set. The classification system employed in GlobeLand30 forms the basis for this mapping study (Table 2).

Table 2. The definition of land cover types.

Types	Description
Cropland	Land used for growing crops, including paddy fields, irrigated land, dry land, vegetable fields, grassland, orchard land, and large plantation land, as well as other lands used for economic tree crops, fruit trees, and crops grown under agroforestry.
Forestland	Land where the tree canopy coverage exceeds 30%, including deciduous broadleaf forests, evergreen coniferous forests, mixed forests, and land with 10-30% tree canopy coverage, such as sparse forests.
Shrubland	Regions where shrub canopy coverage is about 30%, including barren shrubland and mountainous shrubland.
Grassland	Areas dominated by herbaceous vegetation, where plant coverage exceeds 10%, including natural grasslands, grasslands, sparse grasslands, desert grasslands, and urban artificial grassland.
Waterbody	All land-surface water bodies except cropland (paddy fields), wetlands, and perennial snow and ice-covered areas, including rivers, lakes, reservoirs, and ponds.
Bareland	Land with plant coverage lower than 10%, including deserts, sand dunes, rocky land, bare rock, gravel, and areas with biological crust.
Impervious Surface	Land covered by human-made structures, such as buildings, mixed soil, sand, gravel, brick, glass, and other built environments, including residential areas, transportation facilities, and industrial sites.

Wetland	Land located in the boundary between terrestrial and aquatic zones, where water accumulates or where wetland vegetation grows, including inland swamps, lake swamps, river floodplains, marshlands, mangroves, tidal flats, and salt marshes.
Perennial Snow and Ice	Land permanently covered by snow and ice, including areas of high-altitude permanent snow, ice cover, and polar ice caps.

To improve the accuracy and representativeness of the training data, two additional 30-meter resolution datasets were incorporated: the Joint Research Center Global Surface Water (JRC-GSW) and the Global 30 m Impervious Surface Dynamic (GISD30) products. JRC-GSW is developed by time-series Landsat imagery, multiple indices, expert knowledge, and global classification rules. It distinguishes between seasonal and permanent water bodies with an impressive extraction accuracy of 99% for stable water bodies [26]. GISD30 is a five-year global impervious surface product (1985–2020) that uses multi-source remote sensing data to model the dynamic expansion of impervious surfaces. It achieves an overall accuracy of 91.5% and contributes valuable high-precision data to this study [27].

2.4. Validation Dataset

To validate the classification results, 1,200 validation sample points were randomly generated in both Yuli and Linxi counties. These sample points for the years 2020 and 2010 were manually labeled through visual interpretation of time-series Landsat imagery and high-resolution imagery from Google Earth. For quality control, each sample point underwent meticulous review, and those that were ambiguous were excluded from the dataset. At last, 1,097 and 1,101 validation sample points were confirmed for Yuli and Linxi counties, respectively. These datasets are now publicly accessible for broader research use at https://zenodo.org/record/7081098.

For cross-validation, the study also utilized the China Land Cover Dataset (CLCD), a year-by-year land cover dataset for China spanning from 1990 to 2021 [28]. CLCD employs stable training samples extracted from land cover products, combined with manual visual interpretation, to construct a global classification model. The model utilizes time-series Landsat data for year-by-year mapping, which achieves an overall accuracy of 79.31%. Because the spatial resolution of CLCD matches the mapping resolution used in this study, it can serve as a reliable reference for cross-comparison.

3. Methodology

This study focuses on the automated classification and monitoring of land cover in Yuli County, Xinjiang, and Linxi County, Inner Mongolia. The methodology involves the construction of a high-precision, automated training dataset extraction method based on three land cover products: GlobeLand30, GISD30, and JRC-GSW. Using these products, training datasets for 2020 in the selected regions are automatically generated. These datasets are then employed to extract spectral features from time-series Landsat imagery for the baseline year (2020) in each region. A localized classification model is developed through the Random Forest classifier. It is subsequently expanded to other target years, which enables rapid extraction and fine-resolution mapping of land cover products across multiple time periods (Figure 2).

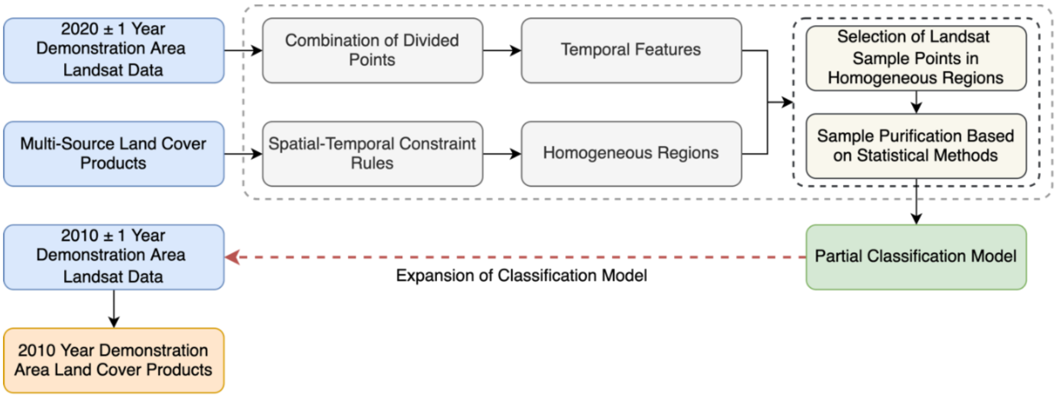

Figure 2. Flow chart for rapid identification and extraction of fine-resolution land cover information.

3.1. Time-Series Feature Extraction

The relatively long revisit period of Landsat, combined with the susceptibility of optical imagery to cloud cover, results in variations in both the quantity and quality of data across different regions. These factors pose challenges for time-series-based land cover mapping [29]. To mitigate these challenges, data processing techniques centered around image compositing have become increasingly important [30]. Two widely used compositing methods are seasonal synthesis (e.g., monthly and quarterly composites) and statistical synthesis (e.g., quantile composites) [31]. Studies show that both methods produce comparable classification accuracy in land cover mapping [32]. However, seasonal synthesis is limited by its reliance on prior knowledge of climatic characteristics, which vary significantly by region and date [16].

This study adopts a quartile synthesis algorithm to enable automated feature extraction, which could compute the 25th, 50th, and 75th percentile composite features for six spectral bands of Landsat data (see Table 1) [16]. Using these synthesized quantile results, four normalized indices are calculated to derive time-series spectral features: Normalized Difference Vegetation Index (NDVI) [33], Normalized Difference Water Index (NDWI) [34], Enhanced Vegetation Index (EVI) [35], and Normalized Burnt Ratio (NBR) [36]. This results in a total of 30 spectral features.

Additionally, recognizing the value of the panchromatic band in providing enhanced spatial texture details due to its higher resolution [23], this study computes three gray-level co-occurrence matrix (GLCM) features: variance, dissimilarity, and entropy. These features are derived from the panchromatic band of the composite image. The computation is performed using a spatial window of 7 × 7. Texture features are integrated into the time-series spectral feature set. Based on the well-established relationship between landform elements and topographic variables [37], this study also incorporates elevation, slope, and aspect data derived from Digital Elevation Models (DEM) into the multi-temporal spectral and texture feature vectors. This integration enhances the model's ability to differentiate between land cover types in the feature space. In total, 42 classification features are selected for this study, incorporating both spectral and topographic data to optimize the classification accuracy.

3.2. Automated Training Data Extraction Methods for Collaborative Multi-Source Land Coverage Products

The quality of training samples plays an important role in determining classification accuracy. It makes the construction of training datasets a focal point in land coverage mapping research [16]. Traditional approaches are time-consuming and labor-intensive, which rely on manual visual interpretation. Thus, they are unsuitable for large-scale land coverage mapping projects. To address this limitation, this study proposes a novel method that synergizes the 30-meter resolution GlobeLand30, JRC-GSW, and GISD30 products to automate the extraction of training data.

However, GlobeLand30 has some limitations, particularly its minimum mapping unit (e.g., 9 × 9 Landsat pixels for wetlands and 4 × 4 Landsat pixels for impervious surfaces). It can result in the omission of fine and fragmented features [10,14]. These features are often fragmented and require more detailed representation, such as roads, village houses, rivers, and other impervious surfaces, water bodies, and wetlands [27,38]. Therefore, this study extracts training data for cropland, forestland, grassland, shrubs, and bare ground based solely on GlobeLand30. For water bodies, wetlands, and impervious surfaces, the study applies a combination of GlobeLand30, JRC-GSW, and GISD30, which demonstrate higher accuracy in capturing these features [14,27].

Firstly, the study integrates information from these three land cover products to identify potential areas for each land cover type. Specifically, GlobeLand30 and JRC-GSW exhibit low commission errors for water bodies. GlobeLand30 reports a 94% user accuracy for water bodies in China [39]. JRC-GSW shows a 0.4% commission rate for water bodies and a 1.4% omission rate for stable water bodies. This study combines the stabilized water body regions extracted by GlobeLand30 and JRC-GSW in 2020. The combined regions define the potential water body region, denoted as P_{water} (Equation 1).

Then, the study considers JRC-GSW's seasonal water bodies, which are mainly composed of wetland types such as floodplains and mudflats, and have a low commission rate (1.4%) [26]. The study integrates the seasonal water body areas from JRC-GSW with the wetlands identified in GlobeLand30 in 2020. Wetland areas outside the potential water body regions are designated as potential wetland areas, denoted as P_{wet} (Equation 2). For impervious surfaces, the study notes the lower omission rate of GISD30 and GlobeLand30. GISD30 reports a producer accuracy of over 90% for impervious surfaces in 2020 [27]. The study integrates the impervious surface areas from both GISD30 and GlobeLand30 in 2020 to define the potential impervious surface area, denoted as P_{Imp} (Equation 3). For cropland, forestland, grassland, shrubland, and bare ground, the potential distribution areas outside the identified water body, wetland, and impervious surface areas are inherited from the GlobeLand30 2020 mapping results.

$$P_{water} = W_{\mathrm{GlobeLand30-Water}} \cup W_{\mathrm{JRC-GSW-P}} \tag{1}$$

$$P_{wet} = (W_{\mathrm{GlobeLand30-Wet}} \cup W_{\mathrm{JRC-GSW-S}}) \cap \neg P_{water} \tag{2}$$

$$P_{Imp} = (Imp_{\mathrm{GlobeLand30}} \cup Imp_{\mathrm{GISD30}}) \cap \neg P_{water} \cap \neg P_{wet} \tag{3}$$

where $W_{\mathrm{GlobeLand30-Water}}$ is the water body in GlobeLand30. $W_{\mathrm{GlobeLand30-Wet}}$ is the wetland in GlobeLand30. $W_{\mathrm{JRC-GSW-P}}$ is the stabilized water body in JRC-GSW; $W_{\mathrm{JRC-GSW-S}}$ is the seasonal water bodies. $Imp_{\mathrm{GlobeLand30}}$ is impervious area in GlobeLand30. Imp_{GISD30} is impervious area in GISD30. $\neg P_{water}$ and $\neg P_{wet}$ are non-water bodies and non-wetland areas.

The land coverage product is particularly well-suited for selecting training data in homogeneous regions due to its higher accuracy in these areas [40]. Therefore, the study calculates the dominant land cover type for a 3 × 3 spatial windows for each class. It could identify the central pixel as a potential homogeneous sample point if all pixels within the window belong to the same class. Homogeneous sample points are further screened from a spectral perspective by calculating the maximum deviation in the spectral values of all pixels within the window for six Landsat bands (blue, green, red, near-infrared, short-wave infrared 1, and short-wave infrared 2). If the polar deviation of all pixels in the 3 × 3 region for the six bands is below predefined thresholds (0.03, 0.03, 0.03, 0.06, 0.03, and 0.03, respectively), the central pixel is deemed a potential homogeneous sample point [13].

For potential homogeneous sample points that meet both spatial and spectral criteria, the intra-class "spectral center of mass" is computed for each object (Equation 4). The absolute spectral distance between each potential pixel and the "spectral center of mass" is then calculated (Equation 5), and the top 60% of potential sample points with the smallest absolute distances are selected as training data [29].

$$C_j = \sum_{i=1}^{n} m_{i,j} / n \tag{4}$$

$$\Delta_{i,j} = |m_{i,j} - C_j| \tag{5}$$

where C_j is the "spectral center of mass" of category j, which is calculated from n potential homogeneous sample points extracted from category j. $m_{i,j}$ and $\Delta_{i,j}$ are the spectral vectors of the potential sample points i in category j and the spectral distances between them and their "spectral centers of mass," respectively. T_j is the set of training samples for category j.

3.3. Construction and Extension of Local Classification Models

A total of 33 spectral features for each Landsat sample point are extracted to build the classification model based on the generated training samples. Previous studies have demonstrated that the Random Forest classifier is highly effective in handling high-dimensional data [15,37] and is robust against noise and feature selection issues. Moreover, the Random Forest model has shown high accuracy and computational efficiency compared to other commonly used classifiers such as support vector machines (SVM), artificial neural networks (ANN), and decision tree-based methods [41–43]. Thus, this study adopts the Random Forest classifier for land cover classification.

The Random Forest classifier relies on two key parameters: the number of classification trees (Ntree) and the number of features considered at each split (Mtry). Previous research suggests that variations in these parameters do not significantly affect classification accuracy [43]. Therefore, following the approach of Chen et al. [37], Ntree is set to 100, and Mtry is defined as the square root of the total number of features used in the training set. This parameter configuration is used to build a localized land cover classification model for the baseline year (2020).

Once the classification model for the baseline year is constructed, it is extended to classify Landsat data from 2010, generating land coverage products for that year. Recognizing the potential radiometric differences between images from different years due to varying imaging conditions and sensor characteristics [27], a correction was applied to ensure data consistency across different years. The relative radiometric normalization method [44] was employed to adjust for radiometric variations between the base year (2020) and the target year (2010), following Equation (6):

$$\rho_r(\lambda_i) = \alpha_i \times \rho_t(\lambda_i) + \beta_i \tag{6}$$

where $\rho_r(\lambda_i)$ is the reflectivity of band λ_i in the base year 2020; $\rho_t(\lambda_i)$ is the reflectivity of band λ_i in the year t to be migrated; and α_i and β_i are the corresponding coefficients of the linear regression model. This process helps to minimize discrepancies caused by different imaging conditions. It ensures that the classification model can be effectively extended across multiple time periods while maintaining the accuracy of land cover classification results.

4. Results

4.1. Results of Automatic Land Cover Classification Mapping

Figure 3 presents the land cover classification results for the two test areas: Yuli County and Linxi County. The automated classification successfully captures the spatial distribution of various land cover types. It closely matches the actual spatial arrangement of features in the imagery. For example, in Yuli County, cropland is primarily concentrated in the western and southern regions, while impervious surfaces are located toward the northwest. In contrast, Linxi County is dominated by extensive grassland and forestland, with cropland primarily distributed along the riverbanks.

The integration of multi-source land cover products during the construction of training datasets significantly enhances the identification of finer features, such as roads and rivers, which are often overlooked in previous land cover products. Moreover, the classification results for both study areas show a notable increase in cultivated land and impervious surfaces in Yuli County, consistent with the findings of Liu Xinping (2019) [45]. In Linxi County, the results indicate a significant decrease in cultivated land, which align with the "Grain for Green" initiative that has been in effect since 2000 [46]. Additionally, the results highlight the expansion of urban areas in Linxi County.

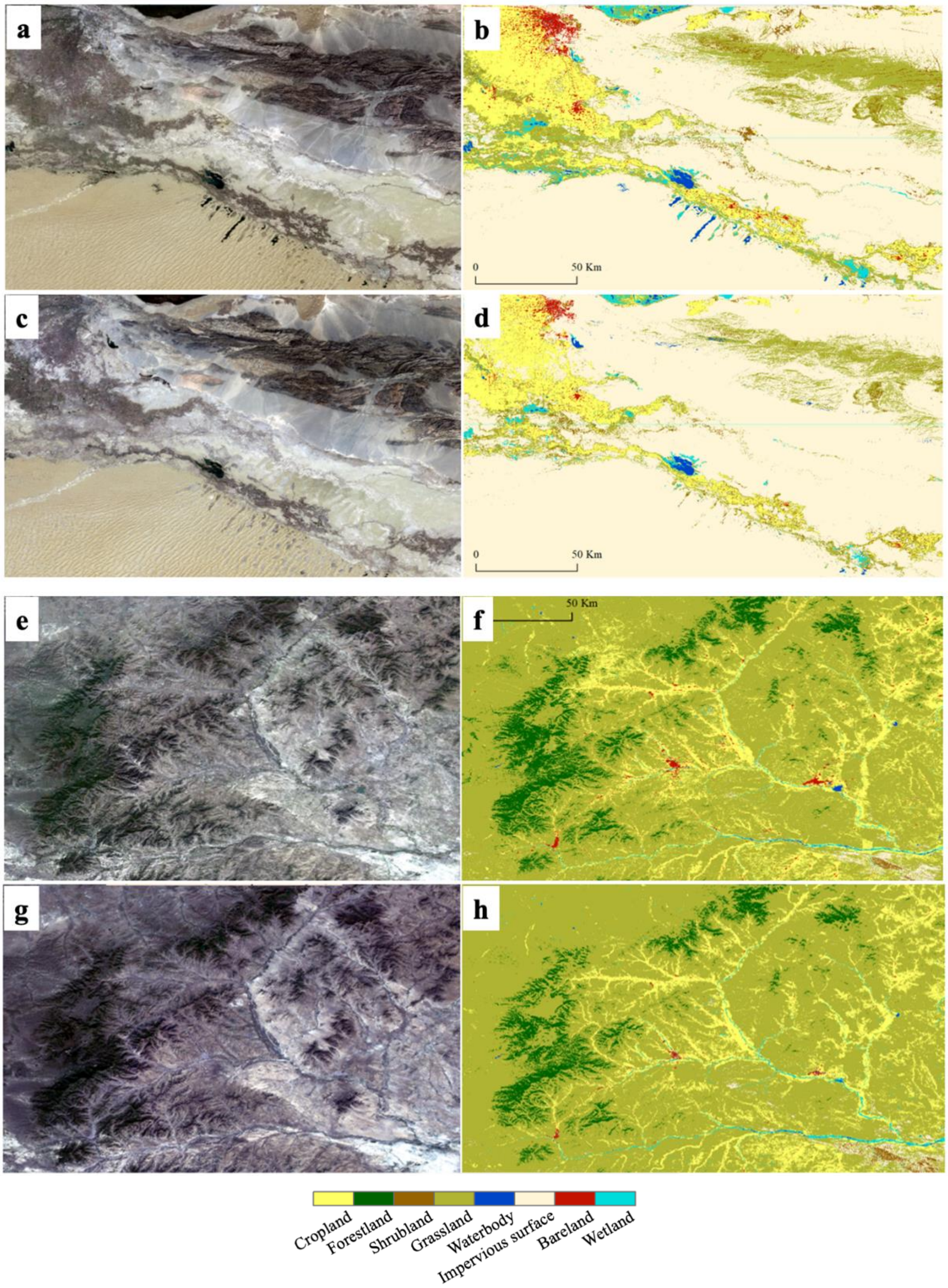

Figure 3. Classification results of two phases of land cover mapping in Yuli County and Linxi County area: (a) RGB image of Yuli in 2020; (b) Land cover mapping results of Yuli in 2020; (c) RGB image of Yuli in 2010; (d) Land cover mapping results of Yuli in 2010; (e) RGB image of Linxi in 2020; (f) Land cover mapping results of of Linxi in 2020; (g) RGB image of Linxi in 2010; (h) Land cover mapping results of Linxi in 2010.

This study also examined the changes in land cover types between 2010 and 2020, and the results are shown in Figure 4. In Yuli County, forestland was notably absent, with bare ground making up the majority of the area. Over the decade, the proportions of several surface types increased: cropland rose from 9.4% to 11.3%, shrubs from 1.1% to 1.9%, grassland from 9.3% to 14.9%, impervious surfaces from 0.7% to 1.3%, water bodies from 0.4% to 0.5%, and wetlands from 0.9% to 1.4%. Meanwhile, the proportion of bare ground dropped significantly. It decreased from 78.3% to 68.7%. In Linxi County, grassland remained the dominant land cover, but there were notable shifts in other surface types. Forestland increased from 5.9% to 8.1%, grassland expanded from 69.0% to 74.0%, and impervious surfaces grew from 0.3% to 0.8%. Meanwhile, cropland saw a significant decline, which decreased from 22.3% to 15.4%. Water bodies always kept around 0.1%. Additionally, the proportions of shrubs, bare ground, and wetlands also decreased, with shrubs dropping from 0.4% to 0.1%, bare ground from 1.3% to 0.8%, and wetlands from 0.8% to 0.6%. These trends highlight the dynamic nature of land cover changes in both regions over the ten-year period.

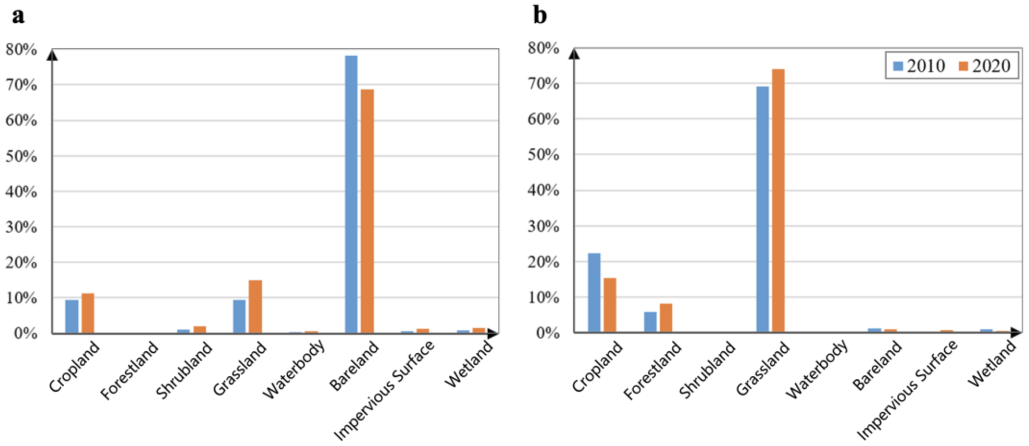

Figure 4. Comparison of percentages of land cover types in 2010 and 2020: (a) Yuli County; (b) Linxi County.

4.2. *Assessment of The Accuracy of Land Cover Mapping Results*

To quantitatively assess the accuracy of the land cover mapping results, four commonly used metrics were employed, including user accuracy, producer accuracy, overall accuracy, and the Kappa coefficient [47]. The accuracy of the land cover mapping for Yuli and Linxi counties is presented in Tables 3 to 6. The overall mapping accuracies for Yuli and Linxi counties in the baseline year (2020) were 92.52% and 90.28%, respectively. For the model expansion year (2010), the mapping accuracies were also high. It reaches 88.33% in Yuli County and 85.28% in Linxi County, which indicates robust results. These findings demonstrate the effectiveness of the proposed methodology, which involves the automatic generation of training data from existing land cover products, the construction of a high-precision classification model, and the temporal expansion of the model for multi-period land cover extraction and monitoring.

It is worth noting that the classification accuracy for shrubs in both regions was relatively low. This could be due to the small proportion of shrubs and the limited number of validation samples in both areas. Additionally, the lower accuracy may be related to the classification performance of GlobeLand30 for shrublands, which was used as the reference product for extracting training data [10]. Interestingly, validation accuracies for bare ground, forestland, and cropland were higher in the model expansion year (2010) compared to the baseline year (2020). In contrast, the accuracies for water bodies, impervious surfaces, and wetlands exhibited more pronounced decreases. Specifically, the producer and user accuracies for water bodies dropped by an average of 13.41% and 15.29% across the two regions. Similarly, the accuracies for impervious surfaces decreased by 20.36% and 8.18%, while wetlands experienced reductions of 15.68% and 19.74%.

Table 3. Evaluation of Mapping Accuracy in Yuli County area in 2020.

Classifier	Crop-land	Shrub-land	Grass-land	Water-body	Bare-land	Impervious surface	Wetland	User accuracy (%)
Cropland	141	0	2	2	6	6	1	89.24
Shrubland	2	6	2	0	2	0	0	50.00

Grassland	11	3	77	0	4	0	5	77.00
Waterbody	0	0	0	45	0	0	2	95.74
Bareland	3	0	10	0	646	4	0	97.43
Impervious surface	3	0	0	0	5	58	0	87.88
Wetland	0	0	0	5	4	0	42	82.35
Producer accuracy (%)	88.13	66.67	84.62	86.54	96.85	85.29	84.00	-

Table 4. Evaluation of Mapping Accuracy in Yuli County area in 2010.

Classifier	**Crop-land**	**Shrub-land**	**Grass-land**	**Water-body**	**Bare-land**	**Impervious surface**	**Wetland**	**User accuracy (%)**
Cropland	125	0	5	0	3	5	1	89.93
Shrubland	2	4	2	0	2	0	0	40.00
Grassland	13	2	78	0	7	8	6	69.74
Waterbody	0	0	1	24	0	0	5	80.00
Bareland	12	3	16	3	676	11	4	93.77
Impervious surface	2	0	0	1	3	38	0	86.73
Wetland	1	0	1	4	4	0	25	71.44
Producer accuracy (%)	80.64	44.44	75.73	75.00	97.27	61.29	60.98	-

Table 5. Evaluation of Mapping Accuracy in Linxi County area in 2020.

Classifier	**Crop-land**	**Forest-land**	**Shrub-land**	**Grass-land**	**Water-body**	**Bare-land**	**Imper-vious surface**	**Wetland**	**User accuracy (%)**
Cropland	127	0	0	35	0	0	6	3	74.27
Forestland	0	97	0	0	0	0	0	0	85.45
Shrubland	0	0	16	0	0	0	0	0	100.00
Grassland	29	2	0	667	0	0	0	0	94.34
Waterbody	0	0	0	0	2	0	0	0	96.67
Bareland	0	0	0	0	0	410	0	0	90.48
Impervious surface	0	0	0	0	0	0	44	0	97.78
Wetland	0	0	0	0	0	0	0	11	78.57
Producer accuracy (%)	81.41	97.92	60.00	92.38	93.55	76.00	86.27	73.33	-

Table 6. Evaluation of Mapping Accuracy in Linxi County area in 2010.

Classifier	**Crop land**	**Forest-land**	**Shrub-land**	**Grass-land**	**Water-body**	**Bare-land**	**Impervious surface**	**Wetland**	**User accuracy (%)**

doi:10.20944/preprints202410.1402.v1

Cropland	135	2	0	47	0	0	5	3	70.31
Forestland	0	84	0	7	0	0	0	0	92.31
Shrubland	0	0	4	0	0	5	0	0	44.44
Grassland	25	11	1	638	0	4	7	2	92.77
Waterbody	0	0	0	2	18	0	0	2	81.82
Bareland	0	0	0	6	0	28	0	0	82.35
Impervious surface	0	0	0	10	0	0	29	0	74.36
Wetland	1	1	0	1	5	0	5	13	50.00
Producer accuracy (%)	83.85	85.71	80.00	89.31	78.26	75.67	63.63	65.00	-

5. Discussion

5.1. Uncertainty Analysis of Automatic Land Cover Classification Based on Model Migration

This study utilized validation data obtained through visual interpretation, where ground cover types remained consistent between 2010 and 2020, to assess the spectral differences between various classes during these two time periods. The goal was to explore the uncertainties inherent in the automatic classification strategy based on the model expansion approach. It is important to note that forestland was not included in the analysis for Yuli County due to its minimal presence in the selected study area.

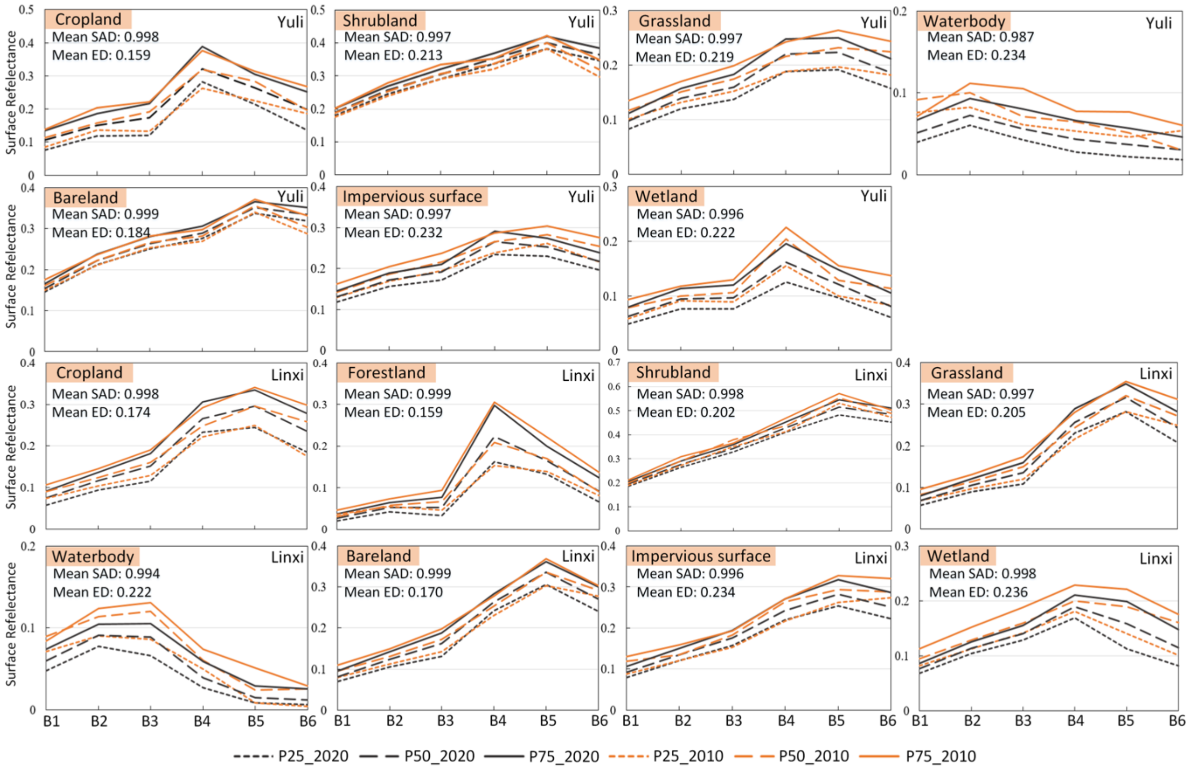

Figure 5. Spectral differences of land cover classes from 2020 to 2010 in Yuli and Linxi county areas after relative radiometric normalization. Noted: B1, B2, B3, B4, B5, B6, B7, and B8 represent Blue, Green, Red, NIR, SWIR1, SWIR2 and Panchromatic bands, respectively; P25_2020、P50_2020、P75_2020 represent the 25th, 50th, and 75th quantile composites in 2020, respectively; P25_2010、P50_2010、P75_2010 represent the 25th, 50th, and 75th quantile composites in 2010, respectively.

doi:10.20944/preprints202410.1402.v1

As shown in Figure 5, the synthesized spectra for the 25th, 50th, and 75th quantiles from 2020 and 2010 demonstrate a high level of agreement, with similar spectral shapes for each class. To quantify this similarity, two widely recognized spectral similarity metrics were applied to the quantile-synthesized data, including Spectral Angle Distance (SAD) and Euclidean Distance (ED) [48]. The analysis showed that the SAD values for the features in both regions exceeded 0.994, while the ED values were consistently below 0.242. This indicates that the spectral consistency between the two periods was generally high, following the application of relative radiometric normalization.

Among all land cover types, cropland and forestland had the highest spectral consistency between 2010 and 2020. In both regions, their mean SAD exceeded 0.998, and mean ED was below 0.174. Bare ground came next, with a mean SAD of 0.999 and mean ED of 0.177. Grassland also showed strong consistency, with mean SAD of 0.997 and ED of 0.212. Shrubland followed closely, with a mean SAD of 0.998 and ED of 0.208. It demonstrates relatively high spectral stability between the two periods. In contrast, water bodies, wetlands, and impervious surfaces showed the least spectral agreement. For water bodies, the mean SAD was 0.991 and ED was 0.228. Wetlands had values of 0.997 and 0.229, and impervious surfaces had 0.997 and 0.233. These results suggest that these classes experienced more spectral variation between 2010 and 2020 compared to other land cover types.

The spectral consistency between the baseline period and the model expansion period has a direct impact on the accuracy of the expanded model [15]. Therefore, the greater spectral variability observed in water bodies, wetlands, and impervious surfaces over time may have contributed to the lower mapping accuracy for these classes following model expansion. This observation is further supported by the validation results presented in Tables 3 and 4. While the mapping accuracy for these features remained high after model expansion, there was a notable decline compared to the baseline year. Thus, the uncertainty in model expansion results is more likely to arise for land cover types that exhibit significant spectral changes over time, such as water bodies, wetlands, and impervious surfaces. These findings underscore the importance of considering temporal spectral variability when expanding land cover classification models to different time periods.

5.2. Assessment of The Importance of Time-Series Classification Features

This study employed a variety of features, including multispectral bands, spectral indices, texture information from panchromatic bands, and topographic data, extracted from time-series Landsat imagery for the classification process. The Random Forest model, known for its ability to quantify the contribution of each feature to classification outcomes via the Gini index [49], enabled the simultaneous evaluation of these diverse features. To better understand how these features influenced the classification results, this study analyzed the relative importance of the 42 features used in the Random Forest model (Figure 6).

The results demonstrate that topographic elevation emerged as the most important classification feature in both Yuli and Linxi counties. Following closely in importance were the 75th quantile composite of the NIR band, the dissimilarity information from the 25th quantile composite of the panchromatic band, the 25th quantile composite of the NBR, and the 50th quantile composite of the NDWI. These features consistently showed high relative importance across both regions. Interestingly, the importance of other topographic features was more variable between the two regions, such as slope and aspect. In Yuli County, where the terrain is relatively flat, slope-related features were less significant. However, in the more mountainous Linxi County, these features gained prominence. It reflects the greater role that topography plays in distinguishing land cover types in regions with complex terrain. On the other hand, the information entropy of the panchromatic data was consistently the least important feature in both study areas. Within the visible spectrum (excluding the NIR band), the features were generally comparable in importance, with the 25th quantile composite of the blue band standing out as the most influential.

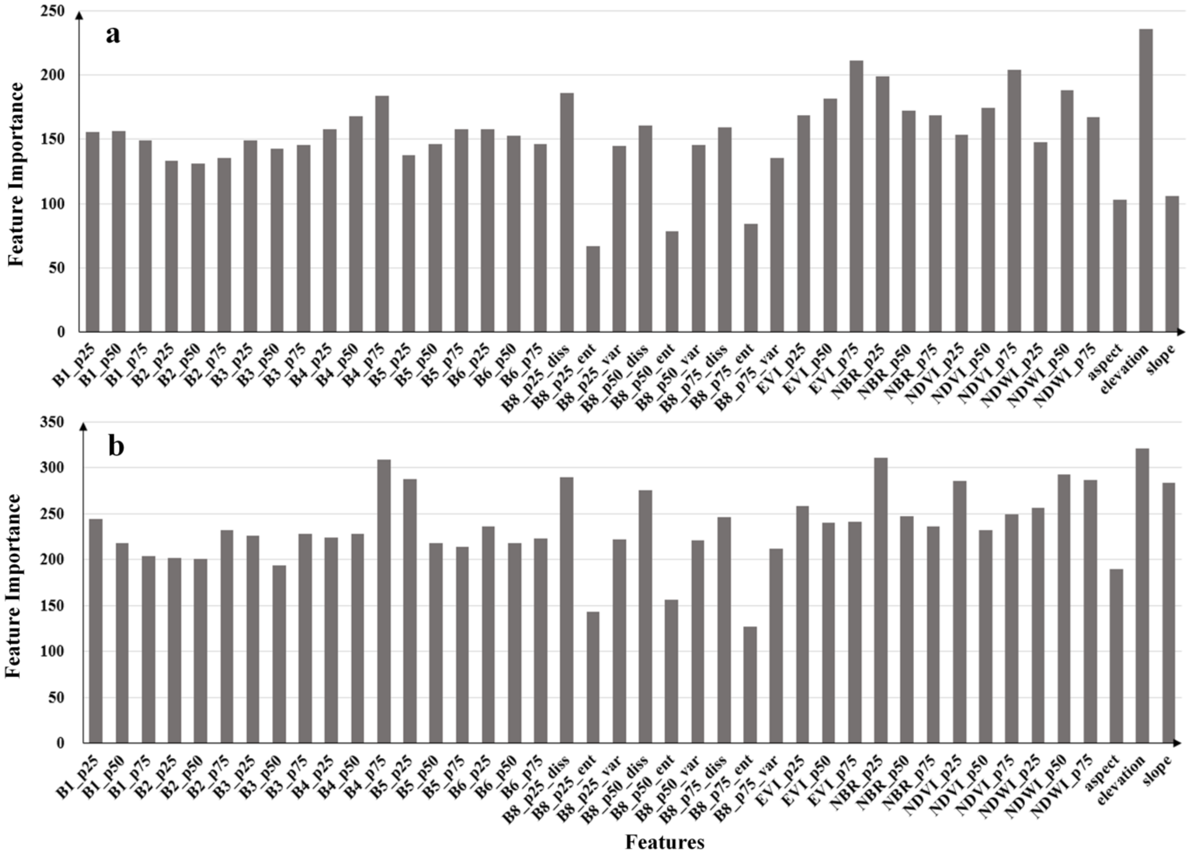

Figure 6. Importance of classification features to land cover mapping results in: (a) Yuli; (b) Linxi. Noted: B1, B2, B3, B4, B5, B6, B7, and B8 represent Blue, Green, Red, NIR, SWIR1, SWIR2 and Panchromatic bands, respectively; P25, P50, and P75 represent the 25th, 50th, and 75th quantile composites, respectively; diss, ent, and var represent the dissimilarity, entropy and variance features, respectively; aspect, elevation, and slope represent angle, elevation and slope, respectively.

When it comes to spectral indices, the importance of the 25th and 50th quantile composites was notably higher than that of the 75th quantile composite in Linxi County, where vegetation is more abundant. This suggests that these composites are particularly effective at distinguishing vegetated from non-vegetated areas in such environments, which represent periods of more robust vegetation growth. In contrast, in Yuli County, which mostly has bare land, the 75th quantile composites of vegetation-related indices like NDVI and EVI held greater significance than the 25th and 50th quantile composites. This pattern aligns with the lower reflectivity (albedo) of vegetation, where the 25th and 50th quantile composites correspond to times of peak vegetation growth, aiding in the differentiation of vegetative and non-vegetative surfaces.

Therefore, the findings indicate that in regions with rich vegetation like Linxi County, the earlier quantile composites (25th and 50th) are more important. Meanwhile, in areas dominated by bare land, like Yuli County, the later quantile composites (75th) play a more important role. This reveals the varying roles that vegetation dynamics and surface characteristics play in influencing classification accuracy across different landscapes.

5.3. Land Coverage Products Cross-Comparison

Using the validation dataset, a cross-comparison was conducted between the 30-meter resolution land cover products—GlobeLand30, CLCD, and the mapping results generated in this study. The quantitative comparisons are outlined in Tables 7 and 8, with the mapping results visualized in Figure 7. The findings reveal that all three products demonstrate commendable accuracy in both study regions, with overall accuracies exceeding 81%. Specifically, in Yuli County, the mapping accuracies of our study for 2020 and 2010 were 92.52% and 88.3%, respectively. By comparison, GlobeLand30 achieved similar accuracies of 90.88% and 88.70%, while CLCD lagged behind with accuracies of 84.05% and 81.68%.

In Linxi County, this study achieved mapping accuracies of 90.28% in 2020 and 85.28% in 2010. GlobeLand30 performed comparably, with accuracies of 90.46% and 88.28%, while CLCD once again trailed with 85.65% and 83.65%. Notably, the classification results from this study closely align with GlobeLand30, while significantly surpassing CLCD. The relatively lower accuracy of CLCD can be attributed, in part, to its reliance on a global classification model, which may not fully capture local land features and characteristics. Previous studies [13] have also highlighted the limitations of global models in accurately representing localized variations.

A closer examination of Tables 7 and 8 shows that CLCD failed to accurately detect wetlands in both study regions. It achieved zero accuracy for this class. This failure is also evident in Figure 7, where CLCD barely identifies wetlands at all. Furthermore, both GlobeLand30 and CLCD exhibit significantly lower producer accuracies for impervious surfaces, water bodies, and wetlands compared to our study. It suggests a tendency for both products to under-detect these specific land classes. In contrast, the mapping results from our study show a higher detection accuracy for impervious surfaces, water bodies, and wetlands, which can be attributed to the strategic integration of multiple land cover products in the construction of the training dataset.

Figure 7 also highlights limitations in GlobeLand30, particularly its omissions of roads and rivers due to its minimum mapping unit constraints. On the other hand, CLCD frequently misclassifies water bodies and wetlands as other land cover types, such as impervious surfaces, especially in the mapping results for Linxi County. In contrast, the methodology of this study ensures more accurate extraction of these features, which combines the strengths of various land cover products. However, it is worth noting that all three products—our mapping results, GlobeLand30, and CLCD—struggled with the accurate extraction of shrubs. It indicates the ongoing challenge of distinguishing this class from other land cover types across diverse regions.

Table 7. The accuracy of three 30 m land-cover products using the validation datasets in Yuli County.

Dataset		**Crop-land (%)**	**Shrub-land (%)**	**Grass-land (%)**	**Water-body (%)**	**Bare-land (%)**	**Imper-vious surface (%)**	**Wetland (%)**	**Overall accuracy (%)**	**Kappa coefficient**
Current Study Results - 2020	User accuracy	89.24	50.00	77.00	95.74	97.43	87.88	82.35	92.52	0.87
	Producer accuracy	88.13	66.67	84.62	86.54	96.85	85.29	84.00		
GlobeLand30 - 2020	User accuracy	89.93	40.00	69.74	80.00	93.27	86.37	71.44	90.88	0.84
	Producer accuracy	80.64	44.44	75.73	75.00	97.27	61.29	60.98		
CLCD - 2020	User accuracy	79.77	0.00	50.00	78.57	94.08	60.78	0.00	84.05	0.72
	Producer accuracy	86.25	0.00	74.73	63.46	97.75	45.59	0.00		
Current Study Results - 2010	User accuracy	92.00	15.00	63.20	80.00	94.70	93.18	77.78	88.33	0.79
	Producer accuracy	74.19	33.33	75.96	75.00	98.12	67.21	63.64		
GlobeLand30 - 2010	User accuracy	85.54	33.33	67.26	67.74	95.01	97.56	77.42	88.70	0.80

	Producer accuracy	91.61	33.33	73.08	65.63	96.39	65.57	54.55		
CLCD - 2010	User accuracy	83.09	100.00	41.28	62.16	92.57	73.68	0.00	81.68	0.67
	Producer accuracy	72.90	11.11	68.27	71.88	95.38	45.90	0.00		

Table 8. The accuracy of three 30 m land-cover products using the validation datasets in Linxi County.

Dataset		**Cropland (%)**	**Forest-land (%)**	**Shrub-land (%)**	**Grass-land (%)**	**Water-body (%)**	**Bare-land (%)**	**Imper-vious surface (%)**	**Wetland (%)**	**Overall accuracy (%)**	**Kappa coefficient**
Current Study Results - 2020	User accuracy	74.27	85.45	100.00	94.34	96.67	90.48	97.78	78.57	90.28	0.82
	Producer accuracy	81.41	97.92	60.00	92.38	93.55	76.00	86.27	73.33		
GlobeLand30 - 2020	User accuracy	71.72	91.95	66.67	95.27	92.86	82.76	85.11	66.67	90.46	0.83
	Producer accuracy	91.03	83.33	40.00	91.97	83.87	96.00	78.43	53.33		
CLCD - 2020	User accuracy	71.75	72.80	0.00	89.40	85.71	75.86	68.75	0.00	85.65	0.73
	Producer accuracy	76.92	95.83	0.00	91.41	77.42	76.00	54.90	0.00		
Current Study Results - 2010	User accuracy	70.31	92.31	44.44	92.70	81.82	82.35	74.36	50.00	85.28	0.74
	Producer accuracy	83.85	85.71	80.00	89.31	78.26	75.67	63.63	65.00		
GlobeLand30 - 2010	User accuracy	73.94	90.24	25.00	90.81	94.12	80.56	87.18	66.67	88.28	0.78
	Producer accuracy	76.25	75.51	20.00	93.72	69.57	90.63	73.91	60.00		
CLCD - 2010	User accuracy	71.75	72.80	0.00	89.40	85.71	75.86	68.75	0.00	83.65	0.70
	Producer accuracy	79.38	92.86	0.00	89.28	78.26	70.97	47.83	0.00		

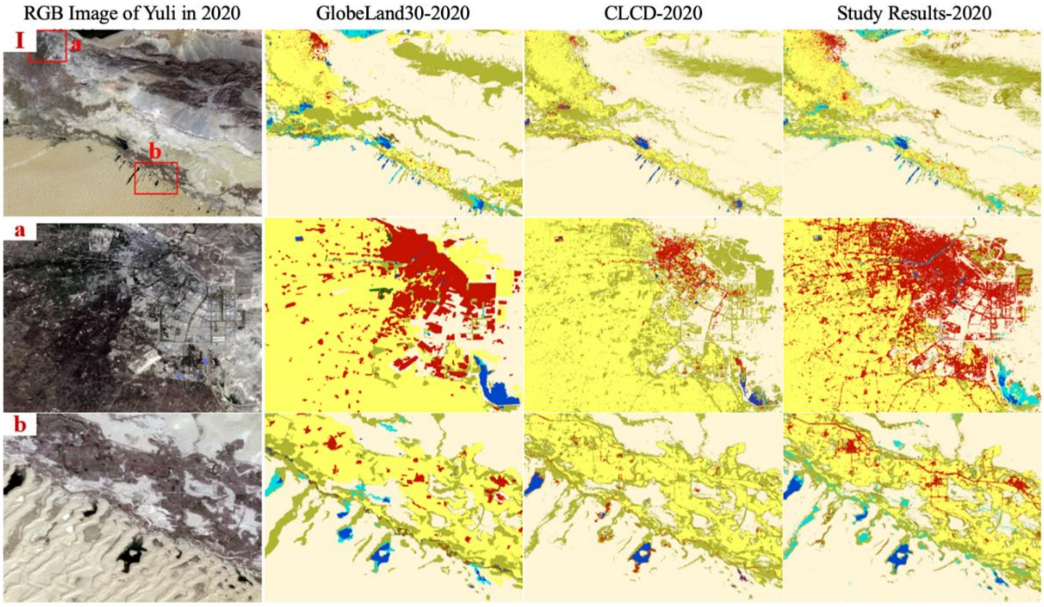
RGB Image of Yuli in 2020
GlobeLand30-2020
CLCD-2020
Study Results-2020
I
a
b
a
b

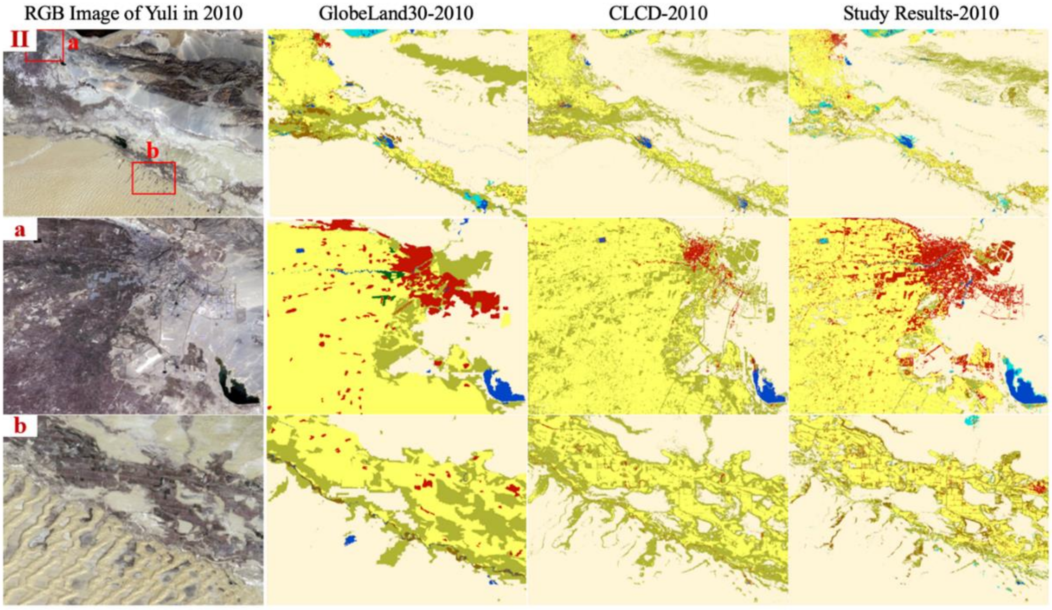
RGB Image of Yuli in 2010
GlobeLand30-2010
CLCD-2010
Study Results-2010
II
a
b
a
b

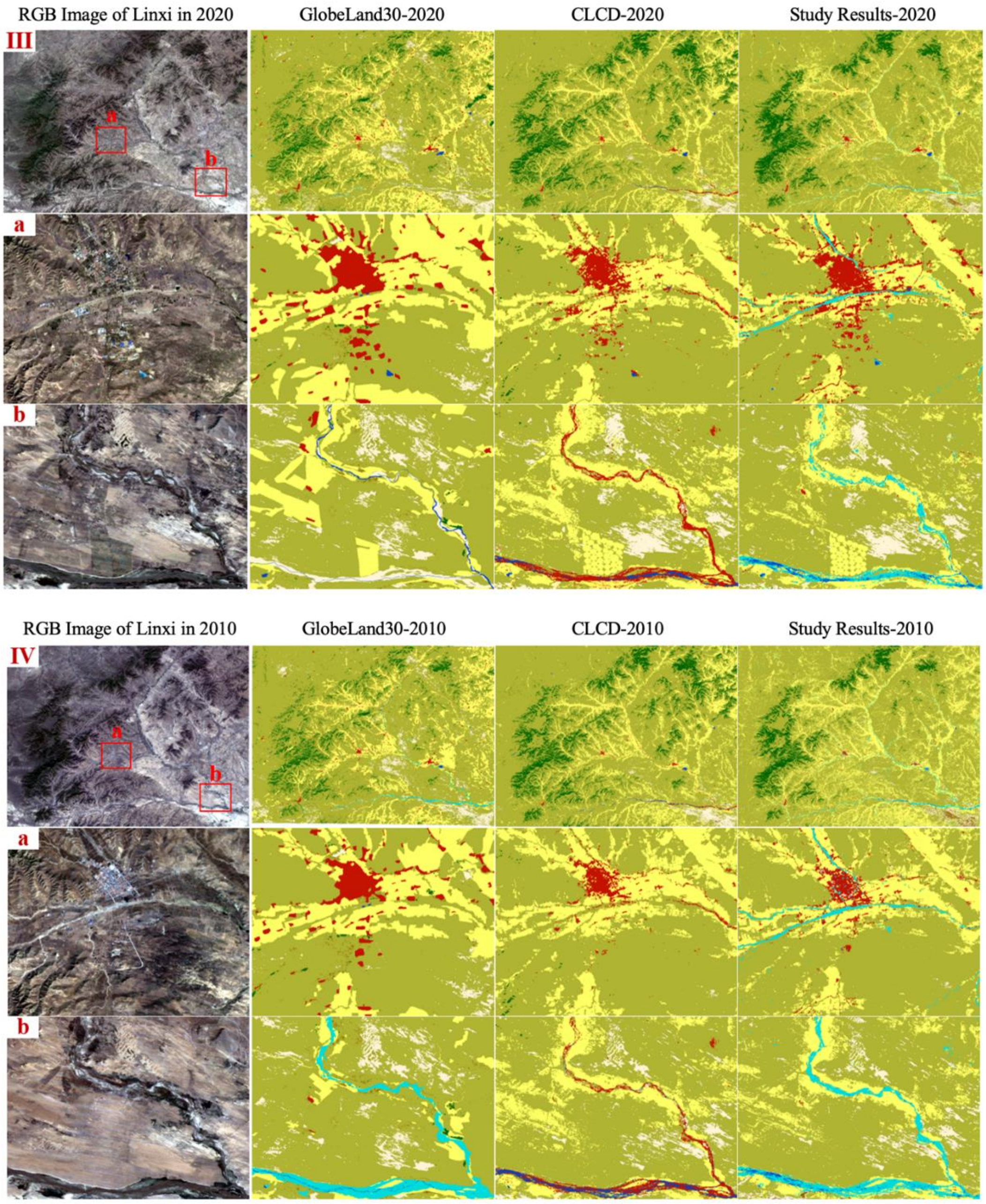

Figure 7. Cross-comparison between the mapping results of our study, GlobeLand30 and CLCD in Yuli and Linxi County areas.

6. Conclusions

This study addresses several critical challenges associated with existing fine-resolution land cover products, such as the heavy reliance on manual input during the mapping process, the difficulty of dynamically updating products, and the limitations in automatically generating multi-period land cover products. To overcome these obstacles, it developed a method that leverages multiple land cover products to automate the extraction of training data and expand the classification model across different time periods. By incorporating these advancements, we conducted an automated identification and monitoring study of land cover elements over multiple years. The proposed methodology was applied and tested in two geographically distinct regions: Yuli County in Xinjiang and Linxi County in Inner Mongolia.

The results of this study demonstrate the effectiveness of our approach, with advanced mapping accuracy in both regions. In Yuli County, the accuracy reached 92.52% in the baseline year (2020) and

88.33% in the expansion year (2010). Similarly, in Linxi County, the mapping accuracy was 90.28% in 2020 and 85.28% in 2010. These results outperform comparable land cover products like GlobeLand30 and CLCD. They highlight the ability of proposed method to provide high-precision, automated land cover classifications over multiple time periods. The automated approach also reduces the need for manual input. This makes land cover map updates faster and more efficient, which is essential for dynamic environmental monitoring.

Despite the advancements, this study highlighted limitations, particularly related to mapping accuracy following model expansion. Features with significant spectral-temporal variability showed higher uncertainty, posing challenges as their spectral signatures change over time, which will impact classification accuracy. Addressing the model's sensitivity to spectral heterogeneity is essential for future research. Efforts will focus on improving the model's ability to handle temporal variability and enhancing its robustness for dynamic landforms. Potential improvements include integrating higher-frequency time-series data, refining spectral correction methods, and utilizing advanced machine learning techniques. Additionally, testing this methodology in diverse regions with varying climates and landscapes will be crucial to assess its generalizability and improve its effectiveness for automated land cover classification.

Thus, this study contributes a significant advancement in the field of remote sensing by providing a scalable, automated approach for generating fine-resolution, multi-period land cover products. The method holds great potential for enhancing the efficiency and accuracy of land cover monitoring, with broad applications in environmental management, land use planning, and climate change adaptation strategies.

Author Contributions: Conceptualization, X.C.; methodology, X.C. and R.C.; software, X.C.; validation, X.C. and Y.R.; formal analysis, X.C. and Y.R.; investigation, Y.R. and R.C.; resources, X.C.; data curation, X.C. and Y.R.; writing—original draft preparation, X.C. and R.C.; writing—review and editing, X.C. and Y.R.; visualization, X.C. and Y.R.; supervision, X.C.; project administration, X.C.; funding acquisition, X.C. All authors have read and agreed to the published version of the manuscript.

Funding: This research was funded by the National Natural Science Foundation of China (42301336), the Open Research Fund of Henan Provincial Key Laboratory of Hydrosphere and Watershed Water Security (grant no. HWWSF202302), and the National Key Research and Development Program of China (2021YFE0117800).

Data Availability Statement: Validation sample points for Yuli and Linxi countie are now publicly shared at https://zenodo.org/record/7081098.

Acknowledgments: In this section, you can acknowledge any support given which is not covered by the author contribution or funding sections. This may include administrative and technical support, or donations in kind (e.g., materials used for experiments).

Conflicts of Interest: The authors declare no conflict of interest.

References

1. Taripanah, F.; Ranjbar, A. Quantitative Analysis of Spatial Distribution of Land Surface Temperature (LST) in Relation Ecohydrological, Terrain and Socio- Economic Factors Based on Landsat Data in Mountainous Area. *Advances in Space Research* **2021**, *68*, 3622–3640, doi:10.1016/J.ASR.2021.07.008.
2. Bolan, S.; Padhye, L.P.; Jasemizad, T.; Govarthanan, M.; Karmegam, N.; Wijesekara, H.; Amarasiri, D.; Hou, D.; Zhou, P.; Biswal, B.K.; et al. Impacts of Climate Change on the Fate of Contaminants through Extreme Weather Events. *Science of The Total Environment* **2024**, *909*, 168388, doi:10.1016/J.SCITOTENV.2023.168388.
3. Mashala, M.J.; Dube, T.; Mudereri, B.T.; Ayisi, K.K.; Ramudzuli, M.R. A Systematic Review on Advancements in Remote Sensing for Assessing and Monitoring Land Use and Land Cover Changes Impacts on Surface Water Resources in Semi-Arid Tropical Environments. *Remote Sensing 2023, Vol. 15, Page 3926* **2023**, *15*, 3926, doi:10.3390/RS15163926.
4. Hansen, M.C.; Reed, B. A Comparison of the IGBP DISCover and University of Maryland 1 Km Global Land Cover Products. *Int J Remote Sens* **2000**, *21*, 1365–1373, doi:https://doi.org/10.1080/014311600210218.
5. Bontemps, S.; Boettcher, M.; Brockmann, C.; Kirches, G.; Lamarche, C.; Radoux, J.; Santoro, M.; Van Bogaert, E.; Wegmüller, U.; Herold, M.; et al. Multi-Year Global Land Cover Mapping at 300 m and Characterization for Climate Modelling: Achievements of the Land Cover Component of the ESA Climate Change Initiative. *The International Archives of the Photogrammetry, Remote Sensing and Spatial Information Sciences* **2015**, *XL-7-W3*, 323–328, doi:10.5194/ISPRSARCHIVES-XL-7-W3-323-2015.

6. Friedl, M.A.; Sulla-Menashe, D.; Tan, B.; Schneider, A.; Ramankutty, N.; Sibley, A.; Huang, X. MODIS Collection 5 Global Land Cover: Algorithm Refinements and Characterization of New Datasets. *Remote Sens Environ* **2010**, *114*, 168–182, doi:10.1016/J.RSE.2009.08.016.
7. Liu, X.; Yu, L.; Sia, Y.; Zhang, C.; Lu, H.; Yu, C.; Gong, P. Identifying Patterns and Hotspots of Global Land Cover Transitions Using the ESA CCI Land Cover Dataset. *Remote Sensing Letters* **2018**, *9*, 972–981, doi:10.1080/2150704X.2018.1500070.
8. Phiri, D.; Simwanda, M.; Salekin, S.; Nyirenda, V.R.; Murayama, Y.; Ranagalage, M. Sentinel-2 Data for Land Cover/Use Mapping: A Review. *Remote Sensing 2020, Vol. 12, Page 2291* **2020**, *12*, 2291, doi:10.3390/RS12142291.
9. Gong, P.; Wang, J.; Yu, L.; Zhao, Y.; Zhao, Y.; Liang, L.; Niu, Z.; Huang, X.; Fu, H.; Liu, S.; et al. Finer Resolution Observation and Monitoring of Global Land Cover: First Mapping Results with Landsat TM and ETM+ Data. *Int J Remote Sens* **2013**, *34*, 2607–2654, doi:10.1080/01431161.2012.748992.
10. Chen, J.; Chen, J.; Liao, A.; Cao, X.; Chen, L.; Chen, X.; He, C.; Han, G.; Peng, S.; Lu, M.; et al. Global Land Cover Mapping at 30 m Resolution: A POK-Based Operational Approach. *ISPRS Journal of Photogrammetry and Remote Sensing* **2015**, *103*, 7–27, doi:10.1016/J.ISPRSJPRS.2014.09.002.
11. Wessels, K.J.; Bergh, F. van den; Roy, D.P.; Salmon, B.P.; Steenkamp, K.C.; MacAlister, B.; Swanepoel, D.; Jewitt, D. Rapid Land Cover Map Updates Using Change Detection and Robust Random Forest Classifiers. *Remote Sensing 2016, Vol. 8, Page 888* **2016**, *8*, 888, doi:10.3390/RS8110888.
12. Radoux, J.; Lamarche, C.; Van Bogaert, E.; Bontemps, S.; Brockmann, C.; Defourny, P. Automated Training Sample Extraction for Global Land Cover Mapping. *Remote Sensing 2014, Vol. 6, Pages 3965-3987* **2014**, *6*, 3965–3987, doi:10.3390/RS6053965.
13. Zhang, H.K.; Roy, D.P. Using the 500 m MODIS Land Cover Product to Derive a Consistent Continental Scale 30 m Landsat Land Cover Classification. *Remote Sens Environ* **2017**, *197*, 15–34, doi:10.1016/J.RSE.2017.05.024.
14. Liu, L.; Zhang, X.; Gao, Y.; Chen, X.; Shuai, X.; Mi, J. Finer-Resolution Mapping of Global Land Cover: Recent Developments, Consistency Analysis, and Prospects. *Journal of Remote Sensing* **2021**, *2021*, doi:10.34133/2021/5289697.
15. Zhang, X.; Liu, L.; Chen, X.; Xie, S.; Gao, Y. Fine Land-Cover Mapping in China Using Landsat Datacube and an Operational SPECLib-Based Approach. *Remote Sensing 2019, Vol. 11, Page 1056* **2019**, *11*, 1056, doi:10.3390/RS11091056.
16. Zhang, X.; Liu, L.; Chen, X.; Gao, Y.; Xie, S.; Mi, J. GLC_FCS30: Global Land-Cover Product with Fine Classification System at 30 m Using Time-Series Landsat Imagery. *Earth Syst Sci Data* **2021**, *13*, 2753–2776, doi:10.5194/ESSD-13-2753-2021.
17. Ahmed, S.F.; Alam, M.S. Bin; Hassan, M.; Rozbu, M.R.; Ishtiak, T.; Rafa, N.; Mofijur, M.; Shawkat Ali, A.B.M.; Gandomi, A.H. Deep Learning Modelling Techniques: Current Progress, Applications, Advantages, and Challenges. *Artificial Intelligence Review 2023 56:11* **2023**, *56*, 13521–13617, doi:10.1007/S10462-023-10466-8.
18. Zhao, S.; Tu, K.; Ye, S.; Tang, H.; Hu, Y.; Xie, C. Land Use and Land Cover Classification Meets Deep Learning: A Review. *Sensors 2023, Vol. 23, Page 8966* **2023**, *23*, 8966, doi:10.3390/S23218966.
19. Capolupo, A.; Monterisi, C.; Tarantino, E. Landsat Images Classification Algorithm (LICA) to Automatically Extract Land Cover Information in Google Earth Engine Environment. *Remote Sensing 2020, Vol. 12, Page 1201* **2020**, *12*, 1201, doi:10.3390/RS12071201.
20. Gray, J.; Song, C. Consistent Classification of Image Time Series with Automatic Adaptive Signature Generalization. *Remote Sens Environ* **2013**, *134*, 333–341, doi:10.1016/J.RSE.2013.03.022.
21. Wang, Y.; Liu, L.; Hu, Y.; Li, D.; Li, Z. Development and Validation of the Landsat-8 Surface Reflectance Products Using a MODIS-Based per-Pixel Atmospheric Correction Method. *Int J Remote Sens* **2016**, *37*, 1291–1314, doi:10.1080/01431161.2015.1104742.
22. Wulder, M.A.; Roy, D.P.; Radeloff, V.C.; Loveland, T.R.; Anderson, M.C.; Johnson, D.M.; Healey, S.; Zhu, Z.; Scambos, T.A.; Pahlevan, N.; et al. Fifty Years of Landsat Science and Impacts. *Remote Sens Environ* **2022**, *280*, 113195, doi:10.1016/J.RSE.2022.113195.
23. Tan, Y.; Xiong, S.; Li, Y. Automatic Extraction of Built-Up Areas from Panchromatic and Multispectral Remote Sensing Images Using Double-Stream Deep Convolutional Neural Networks. *IEEE J Sel Top Appl Earth Obs Remote Sens* **2018**, *11*, 3988–4004, doi:10.1109/JSTARS.2018.2871046.
24. Zhu, Z.; Woodcock, C.E. Object-Based Cloud and Cloud Shadow Detection in Landsat Imagery. *Remote Sens Environ* **2012**, *118*, 83–94, doi:10.1016/J.RSE.2011.10.028.
25. Zhang, X.; Liu, L.; Chen, X.; Gao, Y.; Jiang, M. Automatically Monitoring Impervious Surfaces Using Spectral Generalization and Time Series Landsat Imagery from 1985 to 2020 in the Yangtze River Delta. *Journal of Remote Sensing* **2021**, *2021*, doi:10.34133/2021/9873816.
26. Pekel, J.F.; Cottam, A.; Gorelick, N.; Belward, A.S. High-Resolution Mapping of Global Surface Water and Its Long-Term Changes. *Nature 2016 540:7633* **2016**, *540*, 418–422, doi:10.1038/nature20584.

doi:10.20944/preprints202410.1402.v1

27. Zhang, X.; Liu, L.; Zhao, T.; Gao, Y.; Chen, X.; Mi, J. GISD30: Global 30gm Impervious-Surface Dynamic Dataset from 1985 to 2020 Using Time-Series Landsat Imagery on the Google Earth Engine Platform. *Earth Syst Sci Data* **2022**, *14*, 1831–1856, doi:10.5194/ESSD-14-1831-2022.
28. Yang, J.; Huang, X. The 30m Annual Land Cover Dataset and Its Dynamics in China from 1990 to 2019. *Earth Syst Sci Data* **2021**, *13*, 3907–3925, doi:10.5194/ESSD-13-3907-2021.
29. Xie, S.; Liu, L.; Zhang, X.; Yang, J.; Chen, X.; Gao, Y. Automatic Land-Cover Mapping Using Landsat Time-Series Data Based on Google Earth Engine. *Remote Sensing 2019, Vol. 11, Page 3023* **2019**, *11*, 3023, doi:10.3390/RS11243023.
30. Griffiths, P.; Van Der Linden, S.; Kuemmerle, T.; Hostert, P. Erratum: A Pixel-Based Landsat Compositing Algorithm for Large Area Land Cover Mapping (IEEE Journal of Selected Topics in Applied Earth Observations and Remote Sensing). *IEEE J Sel Top Appl Earth Obs Remote Sens* **2013**, *6*, 2088–2101, doi:10.1109/JSTARS.2012.2228167.
31. Massey, R.; Sankey, T.T.; Yadav, K.; Congalton, R.G.; Tilton, J.C. Integrating Cloud-Based Workflows in Continental-Scale Cropland Extent Classification. *Remote Sens Environ* **2018**, *219*, 162–179, doi:10.1016/J.RSE.2018.10.013.
32. Azzari, G.; Lobell, D.B. Landsat-Based Classification in the Cloud: An Opportunity for a Paradigm Shift in Land Cover Monitoring. *Remote Sens Environ* **2017**, *202*, 64–74, doi:10.1016/J.RSE.2017.05.025.
33. Richardson, A.J.; Wiegand, C.L. Distinguishing Vegetation from Soil Background Information. *Photogramm Eng Remote Sensing* **1977**, *43*, doi:https://www.asprs.org/wp-content/uploads/pers/1977journal/dec/1977_dec_1541-1552.pdf.
34. McFeeters, S.K. The Use of the Normalized Difference Water Index (NDWI) in the Delineation of Open Water Features. *Int J Remote Sens* **1996**, *17*, 1425–1432, doi:10.1080/01431169608948714.
35. Huete, A.; Didan, K.; Miura, T.; Rodriguez, E.P.; Gao, X.; Ferreira, L.G. Overview of the Radiometric and Biophysical Performance of the MODIS Vegetation Indices. *Remote Sens Environ* **2002**, *83*, 195–213, doi:10.1016/S0034-4257(02)00096-2.
36. Miller, J.D.; Thode, A.E. Quantifying Burn Severity in a Heterogeneous Landscape with a Relative Version of the Delta Normalized Burn Ratio (DNBR). *Remote Sens Environ* **2007**, *109*, 66–80, doi:10.1016/J.RSE.2006.12.006.
37. Chen, X.; Liu, L.; Gao, Y.; Zhang, X.; Xie, S. A Novel Classification Extension-Based Cloud Detection Method for Medium-Resolution Optical Images. *Remote Sensing 2020, Vol. 12, Page 2365* **2020**, *12*, 2365, doi:10.3390/RS12152365.
38. Chen, X.; Liu, L.; Zhang, X.; Xie, S.; Lei, L. A Novel Water Change Tracking Algorithm for Dynamic Mapping of Inland Water Using Time-Series Remote Sensing Imagery. *IEEE J Sel Top Appl Earth Obs Remote Sens* **2020**, *13*, 1661–1674, doi:10.1109/JSTARS.2020.2983729.
39. Wang, Y.; Zhang, J.; Liu, D.; Yang, W.; Zhang, W. Accuracy Assessment of GlobeLand30 2010 Land Cover over China Based on Geographically and Categorically Stratified Validation Sample Data. *Remote Sensing 2018, Vol. 10, Page 1213* **2018**, *10*, 1213, doi:10.3390/RS10081213.
40. Yang, Y.; Xiao, P.; Feng, X.; Li, H.; Yang, Y.; Xiao, P.; Feng, X.; Li, H. Accuracy Assessment of Seven Global Land Cover Datasets over China. *JPRS* **2017**, *125*, 156–173, doi:10.1016/J.ISPRSJPRS.2017.01.016.
41. Chutia, D.; Bhattacharyya, D.K.; Sarma, K.K.; Kalita, R.; Sudhakar, S. Hyperspectral Remote Sensing Classifications: A Perspective Survey. *Transactions in GIS* **2016**, *20*, 463–490, doi:10.1111/TGIS.12164.
42. Hasituya; Chen, Z. Mapping Plastic-Mulched Farmland with Multi-Temporal Landsat-8 Data. *Remote Sensing 2017, Vol. 9, Page 557* **2017**, *9*, 557, doi:10.3390/RS9060557.
43. Belgiu, M.; Drăgu, L. Random Forest in Remote Sensing: A Review of Applications and Future Directions. *ISPRS Journal of Photogrammetry and Remote Sensing* **2016**, *114*, 24–31, doi:10.1016/J.ISPRSJPRS.2016.01.011.
44. Hu, Y.; Liu, L.; Liu, L.; Jiao, Q. Comparison of Absolute and Relative Radiometric Normalization Use Landsat Time Series Images. *MIPPR 2011: Remote Sensing Image Processing, Geographic Information Systems, and Other Applications* **2011**, *8006*, 800616, doi:10.1117/12.902076.
45. Liu, X. Changes in Regional Ecosystem Service Values of Land Use/Cover in Yuli County (in Chinese). *Research of Soil and Water Conservation* **2019**, 325–330, doi:https://doc.taixueshu.com/journal/20190164stbcyj.html.
46. Bai, G. Summary Meeting on National Grain for Green Project Acceptance in 2012 Held in Hexigten Banner (in Chinese). *Inner Mongolia Forestry* **2012**, 47–48, doi:10.3969/j.issn.1033-8221.2012.10.038.
47. Olofsson, P.; Foody, G.M.; Herold, M.; Stehman, S. V.; Woodcock, C.E.; Wulder, M.A. Good Practices for Estimating Area and Assessing Accuracy of Land Change. *Remote Sens Environ* **2014**, *148*, 42–57, doi:10.1016/J.RSE.2014.02.015.
48. Ji, L.; Geng, X.; Sun, K.; Zhao, Y.; Gong, P. Target Detection Method for Water Mapping Using Landsat 8 OLI/TIRS Imagery. *Water 2015, Vol. 7, Pages 794-817* **2015**, *7*, 794–817, doi:10.3390/W7020794.
49. Breiman, L. Random Forests. *Mach Learn* **2001**, *45*, 5–32, doi:10.1023/A:1010933404324/METRICS.